Dielectric relaxation dynamics of water and methanol solutions associated with the ionization of N,N-dimethylaniline: Theoretical analyses

AUTHOR(S):

Ando, Koji; Kato, Shigeki

Dielectric relaxation dynamics of water and methanol solutions associated with the ionization of N,N-dimethylaniline: Theoretical analyses

Koji Ando and Shigeki Kato

Citation: The Journal of Chemical Physics **95**, 5966 (1991); doi: 10.1063/1.461618
View online: http://dx.doi.org/10.1063/1.461618
View Table of Contents: http://scitation.aip.org/content/aip/journal/jcp/95/8?ver=pdfcov
Published by the AIP Publishing

Dielectric relaxation dynamics of water and methanol solutions associated with the ionization of *N,N*-dimethylaniline: Theoretical analyses

Koji Ando and Shigeki Kato
Department of Chemistry, Faculty of Science, Kyoto University, Kitashirakawa, Sakyo-ku, Kyoto 606, Japan

(Received 20 June 1991; accepted 5 July 1991)

The solvation dynamics associated with the ionization of *N,N*-dimethylaniline (DMA) in water and methanol solutions has been studied theoretically. Potential energy surfaces of DMA and DMA^+ were computed by *ab initio* molecular orbital (MO) methods. Intermolecular pair potential functions between DMA and H_2O were developed with the aid of the electron distributions of DMA and H_2O and the results of MO calculations for the DMA–H_2O system. Potential functions between DMA and MeOH were also determined empirically using the parameters for DMA–H_2O interaction. Equilibrium and nonequilibrium molecular dynamics calculations were carried out for the DMA–water and DMA–methanol solutions. The simulation results were analyzed comparing two solvents in order to obtain a realistic molecular model for the solvation dynamics of DMA in polar solvents. The solvation coordinate was defined by the potential energy difference between neutral and cation states and free energy curves along it were constructed using the umbrella sampling method. They were found to be well described by parabolas and nonlinear effects such as the dielectric saturation were not observed. The fluctuation–dissipation relation was also examined. It was found that the present systems follow the linear response to a reasonable approximation. In order to provide a kinematic foundation for the choice of the solvation coordinate, the generalized Langevin equation (GLE) for the motion along the solvation coordinate is derived utilizing the reaction path model originally developed to describe photochemical processes in the gas phase. The mechanism of the dielectric relaxation dynamics was discussed on the basis of the quantities in the GLE deduced from the molecular dynamics (MD) calculations.

I. INTRODUCTION

The dielectric relaxation dynamics of polar solvents is one of the most fundamental subjects in solution phase chemistry and has been an active area of research particularly connected with the topic of electron transfer reactions in polar solvents.[1–5] Among theoretical studies on electron transfer in solution, Marcus pioneered to focus on the importance of solvent reorganization free energy in describing the reaction process.[6,7] Since the solution phase chemical reaction is a complex process involving both solute species and a vast number of solvent molecules, it is practically more convenient to examine the reaction free energy surfaces than the potential energy surfaces themselves.[8] Apart from the early theories which stand on the macroscopic continuum approximation, many of current theoretical studies treating nonadiabatic processes such as electron transfer have been applying the potential energy difference between reactant and product states as the microscopic reaction coordinate and examining the free energy curves along it.[9–12] For example, electron transfer reaction in polar solvents may be considered as a surface hopping process between reactant and product surfaces driven by the thermal fluctuation of the solvent. The tunneling of an electron becomes possible when the fluctuation of solvent polarization makes the potential energies of two states coincide with each other. Almost the same theoretical framework can be applied to describe the photoexcitation and ionization processes of solute molecules in solutions using the dressed state representation.[13]

Several theoretical models have been advanced to describe the dielectric relaxation dynamics at a molecular level, e.g., the dynamical mean spherical approximation (MSA) theory,[14–16] the Smoluchowski–Vlasov equation (SVE) theory,[16–18] and the model by van der Zwan and Hynes,[19] and have provided important clues to understand the solvation dynamics. In particular, the model based on the generalized Langevin equation (GLE)[8] is closely related to the interpretation of solvation processes in terms of the free energy curves mentioned above. With this model, the solvation dynamics is represented as the propagation of the system on the free energy curves under the influence of friction and random forces. It must be noted that these theoretical models have been derived on the basis of linear response (LR) theory, in which the dissipation of energy in the nonequilibrium solvation dynamics is replaced by the fluctuation in the equilibrium dynamics. Therefore, it would be a critical test for these theories to examine whether the LR relation holds or not in realistic systems.

Molecular dynamics (MD) simulations will be the most profitable way for such purposes. Several simulation studies on the dielectric relaxation dynamics, which is the subject of the present work, have been reported in recent years. Rao and Berne[20] have observed the nonequilibrium relaxation of the structure of aqueous solvent around an ion just after ionization. Maroncelli and Fleming[21] have analyzed the results of relaxation dynamics of aqueous solvent cluster in

 0021-9606/91/205966-17$03.00

terms of the LR theory. Karim *et al.*[22] have observed the relaxation of solvent water after a sudden change of solute dipole moment and discussed the importance of molecular aspects of the solvent. A simulation study related to electron transfer reaction has been reported by Bader and Chandler.[23] They have investigated the solvent relaxation just after a ferric–ferrous electron transfer in an aqueous solution and examined the LR relation. In the course of the present work, alternative polar solvents other than water have also been examined. Maroncelli[24] has studied acetonitril because it is a simple aprotic solvent and suitable for comparison with analytical models. It seems that both acetonitril and water have been found to follow the LR to a reasonable approximation. On the other hand, the breakdown of the LR relation in methanol (MeOH) solution has been reported by Fonseca and Ladanyi.[25] In all of these studies, solute species are structureless simple spheres or diatomics and some of them with arbitrary potential parameters. Undoubtedly, more extensive works on realistic models of solute species such as polyatomic molecules will be needed.

In the present work, molecular dynamics (MD) trajectory calculations have been carried out for *N,N*-dimethylaniline (DMA) in water and methanol solutions. We focused on the solvation dynamics associated with the ionization of DMA. The solute DMA is known as a prototype of donor molecules in the experimental studies on the photoinduced electron transfer reaction,[26] which is one of the important subjects in organic photochemistry. Besides the interest connected with electron transfer, we can find a significance of examining DMA as the solute, i.e., it may be regarded as an appropriate model of realistic polyatomic organic molecule since it contains an aromatic ring, hydrophobic methyl groups, and an amino N atom which can participate in the hydrogen bonding with protic solvents.

The reason for choosing water and methanol as solvents would be rather obvious. They are most standard and important polar protic solvents studied extensively, both experimentally and theoretically. Although they have close values in intermolecular interaction energies and therefore are expected to show similar static features, the dynamical properties are known to be very different from each other. The qualitative trend of different features between them has been attributed to the longitudinal relaxation time τ_L,[2,27] 0.5 ps for H_2O and 7.7 ps for MeOH,[28] respectively. The time constant τ_L is, however, suitable to interpret the relaxation process with a longer time scale since it is essentially related to macroscopic parameters such as the bulk dielectric relaxation time τ_D and the static and optical dielectric constants. As is known from many experimental and theoretical works,[29,30] more fast components of dielectric relaxation play an important role in describing the dynamics in solutions. It would be, therefore, necessary to examine the microscopic interactions such as the structural forms of the hydrogen bonding network for a satisfactory understanding of the dynamical properties of these solvents.

One of the purposes of the present work is to provide a realistic model for the solvation dynamics of DMA in polar solvents. For this purpose, *ab initio* molecular orbital (MO) calculations were carried out to obtain the intra- and intermolecular potential energy functions. We incorporated the large amplitude motions of the internal degrees of freedom of DMA in the dynamics calculations. Such a calculation based on the realistic model is, to our knowledge, virtually nonexistent despite a number of MD studies that have been performed so far. The other purpose is to analyze the results of MD simulation calculations in terms of the concept of reaction free energy curves. This would give a physically graspable insight into the solvation dynamics. Since the present system is related to the photoinduced electron transfer reactions of organic molecules, this work can be regarded as a first step for the studies on electron transfer reactions in a further stage.

In Sec. II, the intra- and intermolecular potential energy functions are presented. The potential energy surfaces of the isolated DMA and DMA^+ were constructed by *ab initio* MO calculations. With the aid of the electron distribution of DMA (DMA^+) and H_2O and the results of MO calculations for the DMA–H_2O system, we have determined DMA–H_2O pair interaction potential functions. The potential functions for DMA–MeOH interaction were also determined empirically using the potential parameters for the DMA–H_2O interaction. With the potential energy functions developed in Sec. II, we have performed equilibrium and nonequilibrium MD trajectory calculations for DMA–water and DMA–methanol solution systems. The method of calculations, simulation results, and a series of statistical mechanical analyses are presented in Sec. III. In Sec. IV, we discuss the results focusing mainly on the fluctuation–dissipation (FD) relation and the nature of the free energy curves. The generalized Langevin equation (GLE) for the surface hopping process as in the present case is derived utilizing the reaction path model originally developed for photochemical processes in the gas phase.[31] The mechanism of dielectric relaxation processes are discussed on the basis of the GLE derived here. The summary and conclusion of the present work are given in Sec. V.

II. POTENTIAL ENERGY SURFACES

A. Method of calculations

The potential energy surfaces of the isolated DMA and DMA^+ were calculated by *ab initio* MO methods with the restricted Hartree–Fock (RHF) and the unrestricted Hartree–Fock (UHF) approximations.[32] The basis sets we employed are the 3-21G(N*) set and the 6-31G(N*) set. In these basis sets, a set of *d*-polarization functions with the exponent of 0.8 on the N atom is added to the standard 3-21G and 6-31G sets.[33] It is indispensible for describing the amino lone pair orbital of the neutral DMA.

The 3-21G(N*) set was used for the geometry optimizations. The geometries were optimized in C_s symmetry using the analytic energy gradient method for the HF wave function. The optimized wagging angle of the dimethylamino group (θ) was 32.6° for neutral DMA and 0° (planar) for cation DMA. An optimization of the neutral DMA constrained in a planar geometry was also performed. Besides the wagging angle θ, there was little difference in bond distances and bond angles among the results of these calcula-

tions. The most distinct differences in the cation geometry compared with the neutral one were as follows (Fig. 1): (1) the NC_1 bond becomes shortened by 0.05 Å and concommitantly the C_1C_2 and C_1C_3 bonds are extended by 0.03 Å; (2) the NMe_1 and NMe_2 bonds are extended by 0.02 Å; (3) the Me_1NMe_2 bond angle becomes smaller by 2°. The bond distances and the bond angles obtained by these calculations were averaged to be used in the MD trajectory calculations.

The more reliable 6-31G(N*) set was used for the construction of the potential energy surfaces. They are calculated as a function of two internal coordinates; the wagging angle θ and the torsional angle around the NC_1 bond τ. These calculations are carried out at 23 points of (θ, τ); $\theta = 0°$, 10°, 20°, 30°, 40°, 50°, and 60° for $\tau = 0°$ and $\theta = 0°$, 20°, 40°, and 60° for $\tau = 22.5°$, 45°, 67.5°, and 90°. The geometrical parameters other than θ and τ are fixed to the averaged values as mentioned above. The number of basis functions is 109.

B. Potential energy functions of DMA and DMA$^+$

We constructed the potential energy functions of the ground states of DMA and DMA$^+$ using the results of *ab initio* MO calculations described above. Calculated energies were least-squares fitted to the analytic functions

$$V^{\mathrm{DMA}}(\theta,\tau) = \sum_{n=0}^{3}\sum_{m=0}^{3} a_{nm} \cos 2n\tau \cdot \theta^{2m}. \qquad (2.1)$$

As is generally expected, the HF approximation employed here underestimates the ionization potential (I.P.). The calculated adiabatic I.P. was 5.5 eV, whereas the experimental value is reported to be 7.6 eV.[34] We therefore modified the potential energy functions of DMA$^+$ to reproduce the experimental adiabatic I.P. by adding a constant correction term 2.1 eV. By this correction, the vertical I.P. was estimated to be 8.2 eV. The contour maps of the potential energy surfaces are shown in Fig. 2.

The neutral surface is a double well potential for θ, which has a minimum at $(\theta,\tau) = (36°,39°)$ as seen in Fig. 2. The inversion barrier for wagging motion of the dimethylamino group (θ) was 2.5 kcal/mol. The barrier heights for the internal rotation around the NC_1 bond (τ) were 1.3 kcal/mol for the $\tau = 40° \rightarrow 90° \rightarrow 140°$ direction and 2.6 kcal/mol for the $\tau = 40° \rightarrow 0° \rightarrow -40°$ direction, respectively.

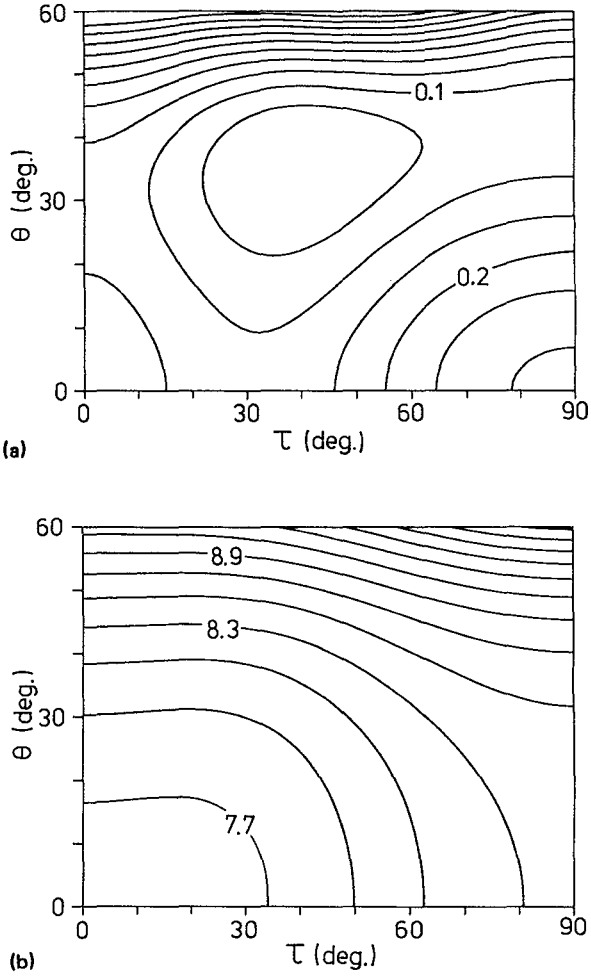

FIG. 2. Contour maps of potential energy surfaces of (a) DMA and (b) DMA$^+$. Energy at the minimum of the DMA$^+$ potential surface is 7.6 eV. Contour spacings are 0.05 and 0.2 eV for DMA and DMA$^+$ potential surfaces, respectively.

The cation surface is a single well potential for θ and is rather steep compared with the neutral surface along both angles. It has a minimum at $(\theta,\tau) = (0°,0°)$ and the rotation barrier for the torsional mode was 16.2 kcal/mol. The parameters for the neutral and cation potential functions are summarized in Table I.

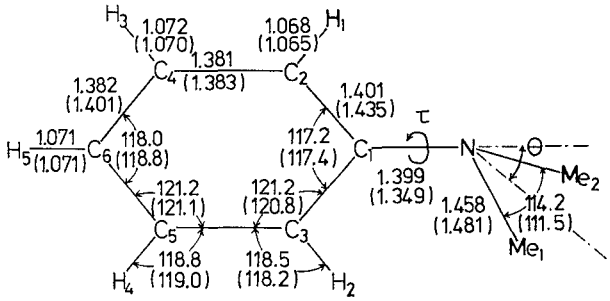

FIG. 1. Geometrical parameters and optimized geometries of DMA and DMA$^+$. Bond distances are in Å and angles in degrees.

C. Intermolecular potential functions

The intermolecular pair potentials between DMA and H_2O were developed with the aid of electron distributions obtained from the MO calculations presented in the previous section. We assumed that the DMA–H_2O interaction potential was described by the sum of the electrostatic and the exchange-exclusion part. The computation of these two parts was implemented by the effective point charge model and the Gordon–Kim model,[35] respectively. Details of these methods have been presented in Ref. 12. We will summarize them below.

The effective point charge model represents the electrostatic term as a sum of Coulombic interactions between the

TABLE I. Parameters of potential energy functions.

	DMA	DMA^+
a_{00} [a]	0.1800	7.6000
a_{10} [a]	0.0816	0.3641
a_{20} [a]	−0.0504	−0.0756
a_{30} [a]	−0.0154	−0.0142
a_{01} [b]	−0.3457	0.8351
a_{11} [b]	−0.2618	−0.1937
a_{21} [b]	−0.0248	0.0373
a_{31} [b]	−0.0068	−0.0583
a_{02} [c]	0.5639	0.4689
a_{12} [c]	0.0916	−0.0481
a_{22} [c]	0.0198	−0.0235
a_{32} [c]	0.0018	0.1007
a_{03} [d]	0.0856	0.0625
a_{13} [d]	0.0143	0.2987
a_{23} [d]	0.0676	−0.0395
a_{33} [d]	−0.0180	−0.0388

[a] Given in eV.
[b] Given in eV rad^{-2}.
[c] Given in eV rad^{-4}.
[d] Given in eV rad^{-6}.

net charges placed on each atom of two molecules. We first calculated the electrostatic potentials of DMA and DMA^+ using the electron density matrices obtained from the MO calculations. The effective charges to be placed on each atom of DMA (DMA^+) were then determined by the least-squares fitting procedure so as to reproduce the calculated electrostatic potentials. We used the values of electrostatic potential at about 500 points around DMA or DMA^+. The contributions from methyl groups were represented by the effective charges on the methyl C atoms.

The exchange-exclusion potential was computed by the Gordon–Kim model. This describes the interaction energy as a function of electron densities of two molecules applying the electron gas model. The electron densities of DMA (DMA^+) and H_2O molecules were approximated by a superposition of net atomic densities using the procedure given in Ref. 12. The methyl groups and CH groups in the phenyl ring of DMA were regarded as the extended atoms. The pair exchange-exclusion potentials were then least-squares fitted to the 12-6 Lennard-Jones functions.

It was found that the effective charges and the parameters of Lennard-Jones functions are rather insensitive to the geometry of DMA (DMA^+). We have therefore taken the values at the geometry $(\theta,\tau) = (40°,0°)$ for DMA and (0°,0°) for DMA^+ and assumed that these values are independent of the angles θ and τ. The results are summarized in Table II. The dipole moment of DMA computed from the resulted effective point charges was 1.5 D, which reproduces the value obtained from the MO calculation. The dipole moment at the geometry $(\theta,\tau) = (40°,45°)$ was 1.2 D from the MO calculation and 1.5 D from the effective charges obtained here, respectively. They are in good agreement with the experimental value of 1.6 D.[36]

TABLE II. Effective point charges on DMA and DMA^+.

	DMA	DMA^+
N	−0.5029	0.1366
C_1	0.4727	0.5539
$C_{2,3}$	−0.4508	−0.6597
$C_{4,5}$	−0.0307	0.0215
C_6	−0.2561	−0.0027
$H_{1,2}$	0.2120	0.3158
$H_{3,4}$	0.1372	0.1664
H_5	0.1475	0.1258
$Me_{1,2}$	0.2017	0.2492

The solute–solvent pair interaction energy was then expressed in the following form:

$$V^{\text{int}} = \sum_a \sum_b \left\{ \frac{q_a q_b}{r_{ab}} + 4\epsilon_{ab}\left[\left(\frac{\sigma_{ab}}{r_{ab}}\right)^{12} - \left(\frac{\sigma_{ab}}{r_{ab}}\right)^{6}\right]\right\}, \tag{2.2}$$

where the subscripts a and b denote the atoms or extended atoms in DMA and H_2O, respectively. We applied the TIP3P (transferable interaction potential) model of liquid water[37] (-0.834 and $0.417e$ for the O and H atoms, respectively) for the effective charges on the H_2O molecule (q_b).

Further we have performed a series of MO calculations for the DMA–H_2O system. We first determined several important configurations of the DMA–H_2O complex using the intermolecular potential functions developed as above. The DMA molecule was put in the planar geometry with its phenyl ring on the xz plane. Three types of configuration of the H_2O molecule were taken into consideration: (A) the C_2 axis of H_2O coincided with that of DMA (z axis) and the H_2O approach from the methyl side of DMA; (B) similar to type (A), but the approach was from the opposite side; (C) the H_2O molecule is constrained on the C_s plane (yz plane) of DMA. The resulting stable configurations for the neutral DMA were as follows: (1) for type (C), one of the H atoms in H_2O is coordinated to the amino lone pair (hydrogen bonding) and the other H atom to the phenyl ring; (2) in terms of the dipole–dipole interaction, the type (A) water coordinates to DMA in profitable direction, whereas the type (B) water is in a disadvantageous direction due to the local attraction from phenyl CH moiety (see Table II).

For the cation case, the O atom of H_2O coordinates to DMA^+ commonly with three types due to the electrostatic attraction from the positive charge which locates mainly on the amino N atom.

Next, we altered the position of the H_2O molecule from the stable point by ± 0.5, ± 1.0, ± 1.5, and ± 2.0 bohrs along the z axis [types (A) and (B)]. For type (C), only the y coordinate of the H_2O molecule was changed as well and the other degrees of freedom (z coordinates and orientational parameters) were optimized. For the configurations of the DMA–H_2O complex thus prepared, a series of *ab initio* MO calculations with RHF and UHF approximations were carried out. The basis set used was the 6-31 G(N*) set for DMA and the 6-31 G(O*) for H_2O, where a set of *d*-

polarization functions with the exponent 0.8 is augumented on the O atom. The number of basis funcions is 128. The intermolecular interaction energies were obtained by

$$V_{\text{int}} = E(\text{DMA–H}_2\text{O}) - E(\text{DMA}) - E(\text{H}_2\text{O}). \quad (2.3)$$

The results were utilized to correct the length and energy parameters σ and ϵ in the Lennard-Jones functions (2.2). After small corrections, we obtained the intermolecular potential curves shown in Fig. 3. The revised Lennard-Jones parameters are summarized in Table III.

In many of the experimental and theoretical studies, solute molecules were conveniently modeled by simple spheres. Considering that the solute radius can be crucial to these approximations, we estimated the effective radius of the solute DMA molecule using the pair potential functions for DMA–H_2O and DMA^+–H_2O developed here. First, the interaction potential excluding the Coulomb term was computed and the length and energy parameters σ and ϵ were evaluated as functions of direction coordinates. The effective mean values of σ and ϵ were computed by the procedure similar to the two-dimensional numerical integration on a surface of sphere using the 26-point quadrature,[38] i.e.,

$$\frac{1}{4\pi h^2}\int\int_{\Sigma} f(x,y,z)d\sigma \approx \sum_{i=1}^{N} \omega_i f(x_i,y_i,z_i), \quad (2.4)$$
$$\Sigma: x^2+y^2+z^2=h^2.$$

Using the same weights ω_i, the mean values were computed by

$$X_{\text{eff}} = \sum_{i=1}^{26} \omega_i X(i\text{th direction}) \quad (X=\sigma,\epsilon). \quad (2.5)$$

The results were $\sigma_{\text{eff}} = 5.0$ Å, $\epsilon_{\text{eff}} = 0.17$ kcal/mol for DMA–H_2O and $\sigma_{\text{eff}} = 5.0$ Å, $\epsilon_{\text{eff}} = 0.14$ kcal/mol for DMA^+–H_2O, respectively. The parameter σ was approximately the same between DMA–H_2O and DMA^+–H_2O. The effective radius of DMA was computed using the Lorentz–Berthelot combining rules. With $\sigma_{\text{DMA-H}_2\text{O}} = 5.0$ Å and $\sigma_{\text{H}_2\text{O-H}_2\text{O}} = 3.15$ Å, $\sigma_{\text{DMA-DMA}}$ was evaluated by $\sigma_{\text{DMA-DMA}} = \sigma^2_{\text{DMA-H}_2\text{O}}/\sigma_{\text{H}_2\text{O-H}_2\text{O}} = 7.9$ Å, thus we get 4.0 Å for the effective radius of DMA. This will be used for comparison between the simulation results and the continuum approximation in Sec. III B and for the normalization of the solvent shell components of the polarization in Sec. III D.

We have also developed the DMA–MeOH and DMA^+–MeOH intermolecular potential functions empirically, using the Lennard-Jones parameters of DMA–H_2O, H_2O–H_2O, and MeOH–MeOH interaction potential functions. For example, the length parameter σ was obtained by

$$\sigma^2_{ac} = \frac{\sigma^2_{ab}}{\sigma_{bb}}\sigma_{cc}, \quad (2.6)$$

where the subscripts a, b, and c denote the atoms or the extended atoms in the DMA, H_2O, and MeOH molecules, respectively. We used the parameters developed by Jorgensen *et al.*[26] for the solvent–solvent intermolecular potential functions; $q_O = -0.834e$, $q_H = 0.417e$, $\sigma_{OO} = 3.15$ Å, and $\epsilon_{OO} = 0.15$ kcal/mol for the H_2O–H_2O interaction and $q_{Me} = 0.265e$, $q_O = 0.700e$, $q_H = 0.435e$, $\sigma_{MeMe} = 3.775$ Å,

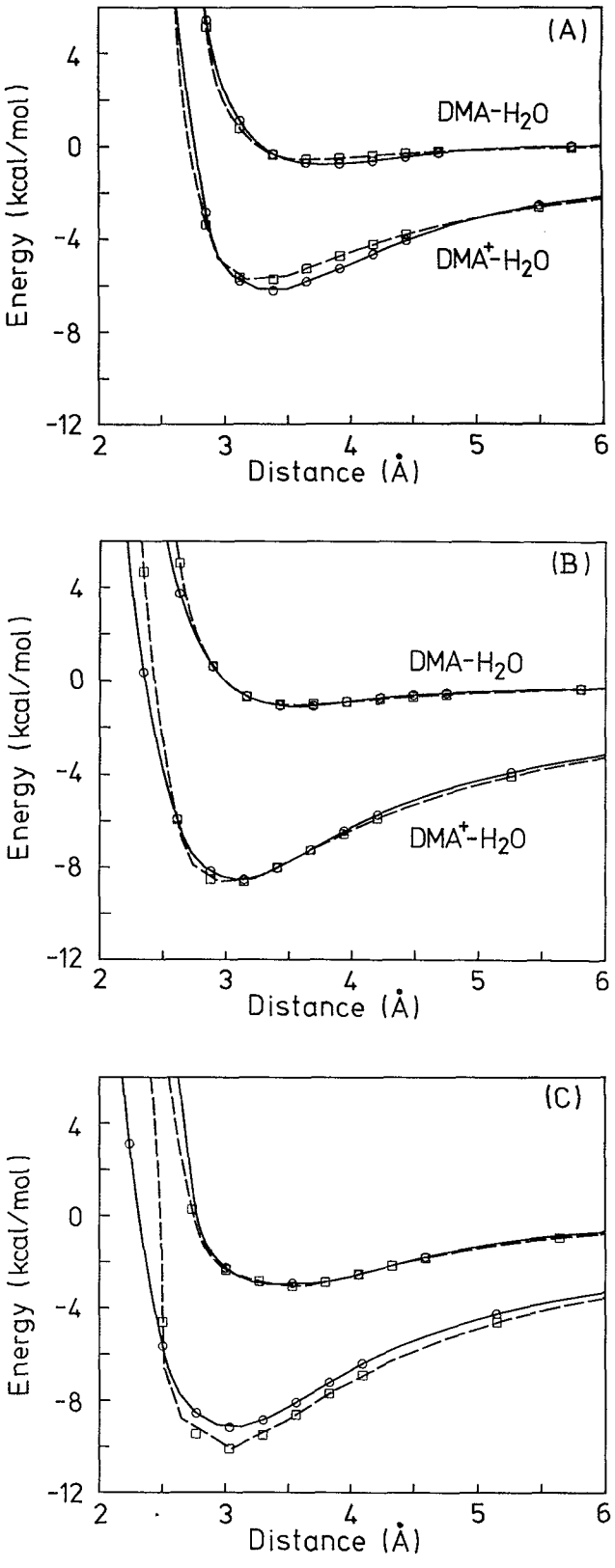

FIG. 3. DMA(DMA^+)–H_2O intermolecular potential energy curves. Symbols ○ (solid lines) are computed values from MO calculations and □ (dashed lines) by Eq. (2.2) with optimized potential parameters. The abscissas denote the distance from the O atom in H_2O to (A) the midpoint of two methyl C atoms; (B) the C_o atom in the phenyl ring; and (C) the NC_1 line of the DMA molecule, respectively. For the types of configurations (A), (B), and (C), see the text.

TABLE III. Lennard-Jones parameters for DMA and DMA^+.

	DMA		DMA^+	
	σ^a	ϵ^b	σ^a	ϵ^b
N	4.584	0.000 60	3.691	0.003 32
C	5.258	0.001 04	4.046	0.007 66
CH	4.978	0.011 15	4.730	0.011 31
Me	4.114	0.038 81	4.828	0.003 97

[a]Given in Å.
[b]Given in kcal/mol.

$\sigma_{OO} = 3.07$ Å, $\epsilon_{MeMe} = 0.207$ kcal/mol, and $\epsilon_{OO} = 0.17$ kcal/mol for the MeOH–MeOH interaction, respectively.

III. MOLECULAR DYNAMICS CALCULATION

A. Method

Both the equilibrium properties and the nonequilibrium relaxation process of ionic solvation were investigated by the classical MD trajectory calculations. The simple three point models of water and methanol, as noted in the previous section, were used as solvents.[37] The solvent molecule is treated as a rigid body. Quaternion parameters were used as the generalized orientational coordinates in order to avoid the singularities in the rotational equations of motion.[39,40] For the solute DMA, we dealt with two internal degrees of freedom explicitly; the wagging angle of the dimethylamino group θ and the torsional angle around NC_1 bond τ. Both of them represent the large amplitude vibrational motions. The internal coordinates other than θ and τ were fixed to the averaged values determined by the procedure described in Sec. II A.

The motion of the solute DMA was described by a classical Hamiltonian

$$H = T_{\rm trn} + \tfrac{1}{2}{}^t\mathbf{p}\mathbf{G}^{-1}\mathbf{p} + \tfrac{1}{2}{}^t\boldsymbol{\omega}\mathbf{I}(\theta,\tau)\boldsymbol{\omega} + W, \tag{3.1}$$

$$\mathbf{G} = \begin{pmatrix} \sum_{i=1}^{N} \frac{\partial x_i^b}{\partial\theta}\frac{\partial x_i^b}{\partial\theta} & \sum_{i=1}^{N} \frac{\partial x_i^b}{\partial\theta}\frac{\partial x_i^b}{\partial\tau} \\ \sum_{i=1}^{N} \frac{\partial x_i^b}{\partial\tau}\frac{\partial x_i^b}{\partial\theta} & \sum_{i=1}^{N} \frac{\partial x_i^b}{\partial\tau}\frac{\partial x_i^b}{\partial\tau} \end{pmatrix}, \quad {}^t\mathbf{p} = (p_\theta, p_\tau),$$

where $T_{\rm trn}$ is the translational kinetic energy, p_θ and p_τ are the conjugate momenta of θ and τ, $\mathbf{I}(\theta,\tau)$ is a 3×3 diagonal inertia tensor, and $\mathbf{x}_i^b$ is the body-fixed coordinate in the frame of the principal axis of inertia with the origin at the center of mass of DMA. The body-fixed coordinate $\mathbf{x}_i^b$ is represented by

$$\mathbf{x}_i^b(\theta,\tau) = \mathbf{U}(\theta,\tau)\mathbf{x}_i^0(\theta,\tau), \tag{3.2}$$

where $\mathbf{x}_i^0$ is the reference coordinate defined in terms of the principal axes at the planar configuration $(\theta,\tau) = (0°,0°)$ and $\mathbf{U}(\theta,\tau)$ a unitary matrix which diagonalizes the inertia tensor obtained from the coordinate $\mathbf{x}_i^0$. $\mathbf{U}(\theta,\tau)$ is a unit matrix for $(\theta,\tau) = (0°,0°)$ and otherwise represented by

$$\mathbf{U} = \mathbf{R}_z\mathbf{R}_x\mathbf{R}_y, \tag{3.3}$$

where $\mathbf{R}_x$ denotes the rotation matrix around the x axis. Three rotation parameters in $\mathbf{U}(\theta,\tau)$ and the principal moments of inertia in $\mathbf{I}(\theta,\tau)$ were represented by two-dimensional spline functions of θ and τ. By this procedure, the Coriolis coupling between the vibrational motions of θ,τ and the rotational motion of the DMA molecule in space are eliminated and the Hamiltonian is written in the form given by Eq. (3.1). The quaternion parameters are utilized to describe the rotational motion of the body-fixed frame of the DMA molecule.

Integration of the equation of motion was performed by the Gear-predictor–corrector method initiated by the fourth order Runge–Kutta method. The five- and four-value Gear algorithms[41] were applied for the first- and second-order equations of motion, respectively. The periodic boundary condition was applied. Each cubic cell contains one DMA and 250 H_2O or 216 MeOH molecules. The mass density was set to be 1.0 and 0.759 g/cm^3 for water and methanol solutions, respectively. The value for methanol is taken from Ref. 37(b), where the mass density has been calculated by the constant pressure Monte Carlo simulation using the same potential functions as used in the present work. The simulation box lengths were then 19.7 (water) and 24.9 Å (methanol), respectively. The long-ranged Coulomb term in the solvent–solvent interaction potential was calculated using the Ewald's summation technique. The surface term was included in the sum in which the experimental values of the dielectric constant were used (78.4 and 33.7 for water and methanol, respectively).

As is generally recognized, it is not adequate to apply the periodic boundary condition to the calculations of the solute–solvent interaction especially for such systems as the present in which the total charge in the simulation box is not zero. We have implemented the potential tapering method[42] for the computation of the solute–solvent interaction and estimated the energetic contribution from outside the tapered sphere by the continuum approximation. The tapering function we adopted was

$$\sigma(\xi) = \begin{cases} 1 & \text{for } \xi < 0 \\ 1 - \xi^3[10 - \xi(15 - 6\xi)] & \text{for } 0 < \xi < 1, \\ 0 & \text{for } \xi > 1 \end{cases} \tag{3.4}$$

$$\xi = (R_{\rm c.m.} - R_T)/(R_C - R_T),$$

where $R_{\rm c.m.}$ denotes the distance between the centers of mass of the solvent and solute molecules. We took the cut-off distance R_C at half of the simulation box length and $R_T = 0.9\,R_C$. The function $\sigma(\xi)$ smoothly damps the bare atom–atom pair potential function V by

$$U_{ab} = \sigma(R_{\rm c.m.})V_{ab}. \tag{3.5}$$

We have estimated the contribution from the region outside the tapered sphere by the continuum approximation (Born formula), in which we used the experimental values for the dielectric constant and the computed value for the dipole moment of DMA (1.5 D) and $(R_C + R_T)/2$ for the radius of the sphere, respectively.

The equilibrium MD calculations consisted of 20 (water) and 40 ps (methanol) runs after several 10 ps of cooling and equilibration runs. The time steps used were 0.4 and 0.5 fs for water and methanol solutions, respectively. Good energy conservation ($\Delta E < 0.3$ kcal/mol) was achieved. We

found that the most part of errors comes from cutting off the short-ranged (Lennard-Jones) term in the solvent–solvent pair interaction potential with the minimum image convention. No temperature control algorithm was used in all the equilibrium and nonequilibrium simulations.

B. Static properties

Before proceeding to the dynamics, we are going to present the results of the equilibrium simulations and discuss the static properties of the present systems. A summary of the results obtained are listed in Table IV.

The difference between the solvation energies of DMA and DMA$^+$, given as the average of the solute–solvent interaction energy, were 104.2 and 91.9 kcal/mol in water and methanol solvent, respectively. We have also estimated the solvation energies using the continuum approximation and compared them to the simulation results. The solvation energies of a dipole and an ion in a spherical cavity with radius R which is immersed in the continuum dielectric with the static dielectric constant ϵ were computed by

$$V_0^{\text{cont}} = -\frac{2(\epsilon-1)}{2\epsilon+1}\cdot\frac{\mu^2}{R^3}, \tag{3.6}$$

$$V_1^{\text{cont}} = -\frac{q}{R}\left(1-\frac{1}{\epsilon}\right). \tag{3.7}$$

When we adopt 4.0 Å and 1.5 D for the effective radius (R) and the dipole moment (μ) of DMA (Sec. II C), the solvation energies are largely underestimated as shown in Table IV. These deviations are naturally attributable to the contribution from the local or microscopic interactions between the DMA molecule and the nearest-neighbor solvent molecules.

The structural character of solvation will be reflected in the solute–solvent radial distribution functions (rdfs). Though we have computed all the atom–atom rdfs, only the center-of-mass (c.m.)–c.m rdfs are presented in Fig. 4. The solid and dashed lines correspond to DMA and DMA$^+$, respectively. The radial distribution for the DMA–H_2O system has a first main peak centered at 5.8 Å, which is a reasonable value since the effective radii of DMA and H_2O were estimated as 4.0 and 1.6 Å, respectively. Behind this peak is seen a minimum located at about 7.0 Å, which was adopted for the definition of the first solvation shell boundary (r_{shell}). We can also see in the figure that the distribution for DMA–H_2O has a tail or shoulder in the region from 3 to 4 Å. This is due to the hydrogen bonding of H_2O molecules

TABLE IV. Results from equilibrium MD simulations.

Solvent	H_2O		MeOH	
solute	DMA	DMA$^+$	DMA	DMA$^+$
Temperature[a]	300 ± 8	298 ± 9	297 ± 9	299 ± 9
$\langle V^{\text{int}}\rangle$[b]	-10.4	-114.6	-6.8	-98.7
$\langle V^{\text{cont}}\rangle$[b]	-0.5	-82.0	-0.5	-80.6
$\langle N_{\text{shell}}\rangle$	41 ± 2	40 ± 2	23 ± 2	24 ± 2

[a] Given in K.
[b] Given in kcal/mol.

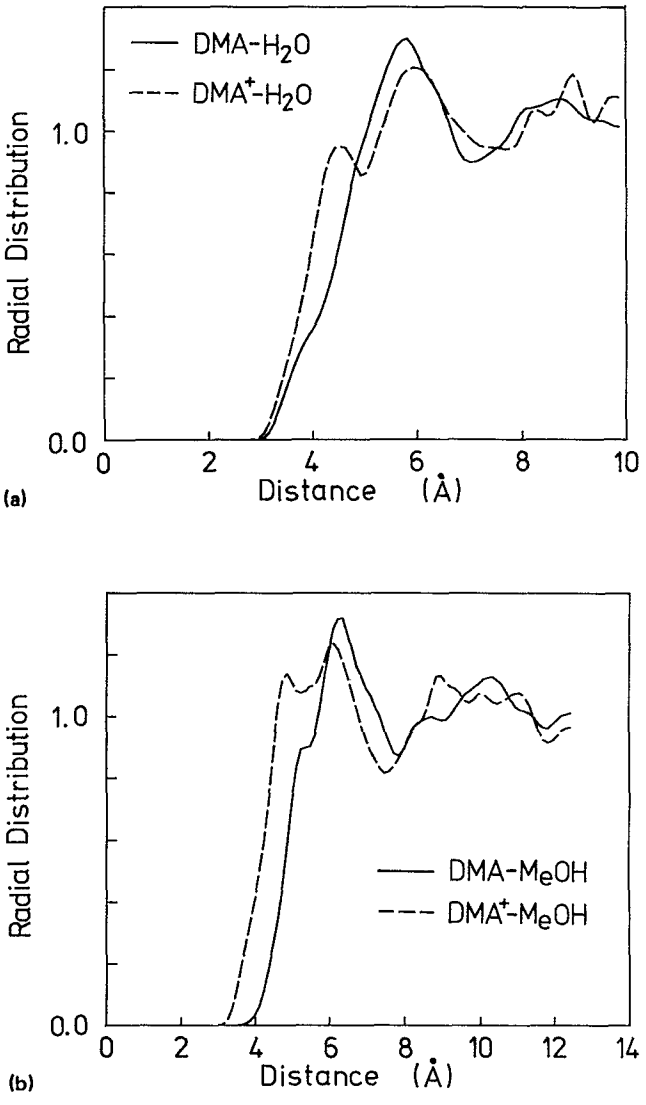

FIG. 4. Radial distribution functions between centers of mass of DMA(DMA$^+$) and (a) H_2O and (b) MeOH. Solid and dashed lines correspond to DMA and DMA$^+$, respectively.

to the amino N atom and the aromatic ring of DMA.

A splitting of the main peak was observed in the radial distribution for the DMA$^+$–H_2O system. These peaks are centered at 4.5 and 5.9 Å, respectively. The former reflects the coordination of water molecules at above the aromatic ring plane of DMA$^+$. The latter peak partly comes from a relatively pronounced coordination around the methyl groups of DMA$^+$.

The rdfs for DMA–MeOH and DMA$^+$–MeOH systems have roughly similar features to those observed in the case of aqueous solution. The first peak in DMA–MeOH radial distribution is centered at 6.3 Å and the minimum behind it at 7.8 Å (r_{shell}). Two peaks are found at 4.8 and 6.1 Å in the DMA$^+$–MeOH distribution. In contrast to the DMA–H_2O case, tails or shoulders in the small r region were not observed in the DMA–MeOH radial distribution curve.

As mentioned above, the first solvation shell boundary was defined using the minima in the rdfs of the neutral systems. With this shell radius r_{shell}, we have estimated the averaged number of solvent molecules $\langle N_{\text{shell}} \rangle$ inside the first solvation shell. There were about 40–41 H_2O or 23–24 MeOH molecules inside the first shell around the solute DMA molecule.

C. Potentials of mean force

Beginning with the electron transfer reaction, chemical reactions in solution are discussed on the basis of the reaction free energy surfaces rather than the potential energy surfaces. We have investigated the potentials of mean force, or the free energy curves along the solvation coordinate s which is defined by

$$s = f(\mathbf{R},\mathbf{r}) = W_1(\mathbf{R},\mathbf{r}) - W_0(\mathbf{R},\mathbf{r}), \tag{3.8}$$

where W_0 and W_1 are the potential energies for the system with neutral and cation DMA, and $\mathbf{R}$ and $\mathbf{r}$ the coordinates of solute and solvent molecules, respectively. The potential energy consists of three terms

$$W_I = V^{\text{solv}}(\mathbf{r}) + V_I^{\text{DMA}}(\mathbf{R}) + V_I^{\text{int}}(\mathbf{R},\mathbf{r}) \quad (I = 0,1). \tag{3.9}$$

With the definition (3.8), the potential energies of two states always coincide at $s = 0$.

The equilibrium MD calculations are carried out with the Hamiltonian

$$H = T + W_0 + \alpha(W_1 - W_0). \tag{3.10}$$

With $\alpha = 0$ and 1, the system evolves on the neutral and cation potential surfaces, respectively. As will be described below, the interpolation between the two free energy curves (neutral and cation) becomes feasible with $0 < \alpha < 1$, which may be regarded as the umbrella sampling method.

The probability density for the solvation coordinate s including α as a parameter is

$$P(s;\alpha) = \frac{\int \delta[s - f(\mathbf{R},\mathbf{r})] \exp\{-\beta[W_0 + \alpha(W_1 - W_0)]\} d\mathbf{R}\, d\mathbf{r}}{Z_\alpha}, \tag{3.11}$$

$$Z_\alpha = \int \exp\{-\beta[W_0 + \alpha(W_1 - W_0)]\} d\mathbf{R}\, d\mathbf{r}, \tag{3.12}$$

where $\beta = 1/k_B T$ and k_B the Boltzmann constant. We can compute $P(s;\alpha)$ directly from the equilibrium simulation on the potential $W_0 + \alpha(W_1 - W_0)$. The free energy curve $F(s;\alpha)$ for the coordinate s is defined by

$$F(s;\alpha) - F(s;0) = -k_B T \ln[Q(s;\alpha)/Q(s;0)], \tag{3.13}$$

where the partition function $Q(s;\alpha)$ is given by

$$Q(s;\alpha) = \int \delta[s - f(\mathbf{R},\mathbf{r})] \times \exp\{-\beta[W_0 + \alpha(W_1 - W_0)]\} d\mathbf{R}\, d\mathbf{r}. \tag{3.14}$$

From Eqs. (3.8)–(3.14), the following simple but important relation is derived:

$$F(s;\alpha) - F(s;0) = \alpha s. \tag{3.15}$$

It is computationally convenient to use $P(s;\alpha)$ than $Q(s;\alpha)$. We get

$$F(s;\alpha) - F(s;0) = -k_B T \ln[P(s;\alpha)/P(s;0)] + C, \tag{3.16}$$

$$C = -k_B T \ln\langle \exp[-\beta\alpha(W_1 - W_0)] \rangle_0 = +k_B T \ln\langle \exp[+\beta\alpha(W_1 - W_0)] \rangle_\alpha. \tag{3.17}$$

We now consider the crossing between two free energy curves; one for the cation state and the other for the photon dressed neutral state. With

$$Q(s;0') = \int \delta[s - f(\mathbf{R},\mathbf{r})] \times \exp[-\beta(W_0 + V_{\text{photon}})] d\mathbf{R}\, d\mathbf{r} \tag{3.18}$$

and

$$Q(s;0) = \int \delta[s - f(\mathbf{R},\mathbf{r})] \exp(-\beta W_0) d\mathbf{R}\, d\mathbf{r}, \tag{3.19}$$

we obtain the relation

$$F(s;0') = F(s;0) + V_{\text{photon}}. \tag{3.20}$$

Suppose we have computed $F(s;0)$ by $F(s;0) = -k_B T \ln P(s;0)$ and found its minimum at $s = s_0$ [Fig. 5(b)]. The ionization potential (I.P.) in solution is defined by the value of V_{photon} necessary to make $F(s;0')$ cross at its minimum with $F(s;1)$, as shown schematically in Fig. 5(a), under an assumption that the energy of the emitted electron is zero. We can derive a simple relation I.P. $= s_0$ straightforwardly. [From Eq. (3.15), $F(s;1)$ and $F(s;0')$ cross at $s = 0$. Thus replacing s by $s - s_0$, we make $F(s;0')$ cross with $F(s;1)$ at its minimum. This means $s = W_1 - (W_0 + s_0)$ which shows that s_0 is just the photon energy needed.] The computed values of the I.P. of DMA in solution were 6.5 and 7.0 eV in water and methanol solutions, respectively. Compared with the vertical I.P. for the isolated DMA (8.2 eV), the I.P.'s are lowered by the interaction with the solvents in solutions.

Figure 6 shows the free energy curves $F(s;1)$ and $F(s;0')$. The dressing energy for $F(s;0')$ was taken so that the neutral curve crosses with the cation curve at $s = s_1$ as shown in Fig. 5(b), which is regarded as the thermal threshold for transition. The interpolation between two curves was realized by the umbrella sampling method with $\alpha = 0.5$. The symbols □, △, and × correspond to the equilibrium simulations with the charge parameters $\alpha = 0$, 1, and 0.5, respectively. The free energy differences ΔF between the crossing point and the minimum of the cation curve were 1.5 (water)

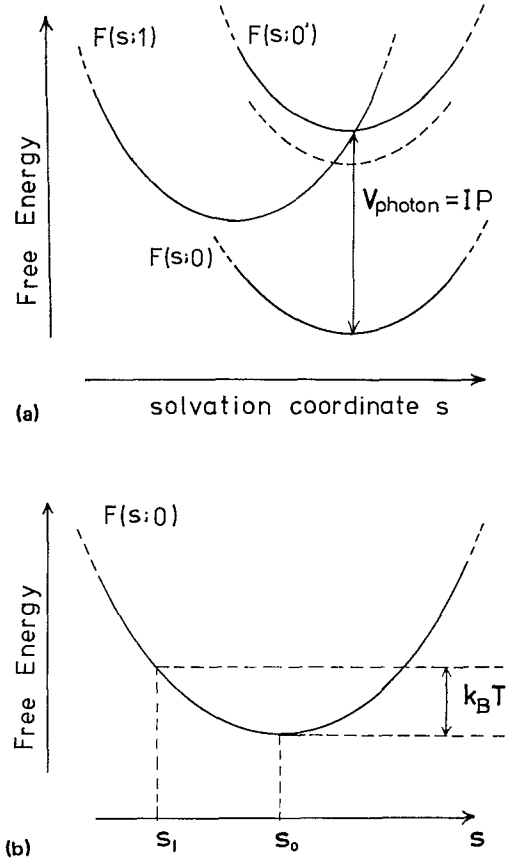

FIG. 5. Schematic representations of free energy curves. (a) Definition of the ionization potential (I.P.) in solution. (b) Free energy minimum s_0 and thermal threshold s_1 (k_B is the Boltzman constant). For details, see the text.

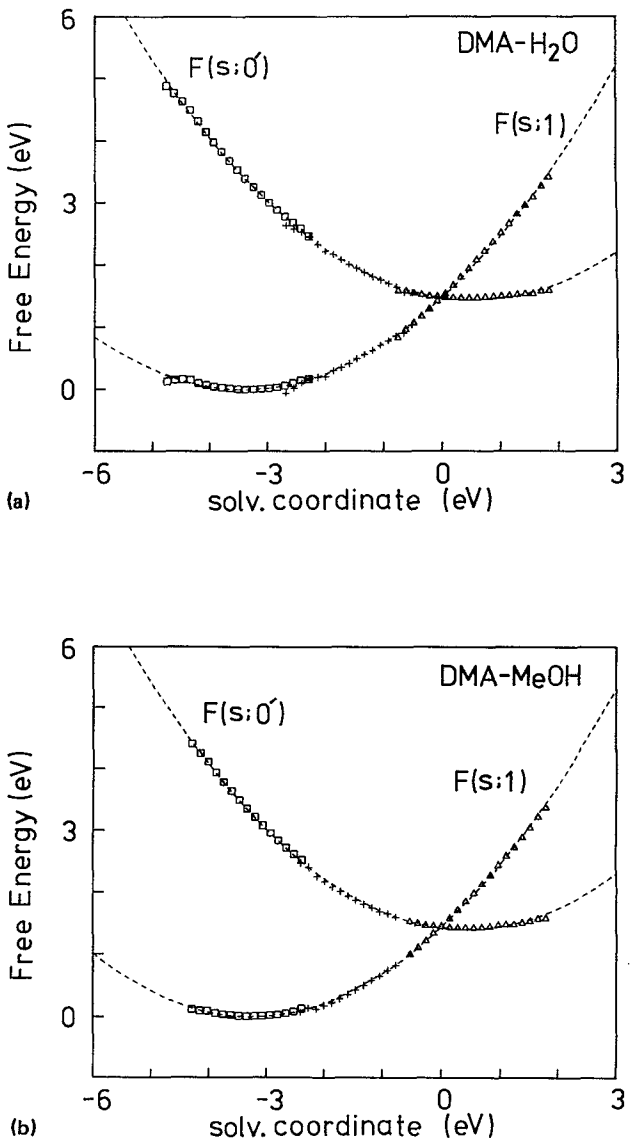

FIG. 6. Free energy curves along the solvation coordinate in (a) water and (b) methanol solutions. Symbols □, △, and × correspond to the charge parameter $\alpha = 0,1$ and 0.5, respectively. Dashed lines are least-squares fitted parabolas.

and 1.4 eV (methanol). The changes of the solvation coordinate Δs were 3.4 (water) and 3.2 eV (methanol).

We have estimated the force constants, or curvatures of the free energy curves by least-squares fitting. As is obvious from Eq. (3.15), the force constants for the neutral and cation curves must be the same if the curves are exactly parabolic. We have attempted a fitting to describe the whole region of two curves by parabolas with a single force constant using Eq. (3.15). The fitted curves were presented by the dashed lines in Fig. 6, the force constants of which were 0.25 (water) and 0.27 eV^{-1} (methanol). Recently, the validity of two assumptions, the parabolic free energy curves and the solute independence of force constants, has been examined by several authors. These assumptions have been predicted from the continuum dielectric models and commonly adopted in many of the early works. Carter and Hynes[13,43] and Kakitani *et al.*[44] have discussed the nonlinearity of solvation related to the electron transfer in solution. As seen in Fig. 6, the free energy curves $F(s;0)$ and $F(s;1)$ are well approximated by parabolas with the same force constants and nonlinear effects such as the so-called dielectric saturation are not observed for both the solvents in the present calculations. It is noted that nonparabolic free energy curves can be obtained for the case where the charge distribution in solute molecule depends strongly on its geometry.[12]

We can see in Fig. 6 that the curves for the two solvents are quite similar to each other. As seen from the definition (3.8)–(3.14), the free energy curve reflects the thermal fluctuation of the solvation coordinate s. The difference between the absolute values of both the solute–solvent and solvent–solvent pair interaction energies in these two solvents is small, which may be rationalized from the values of the dipole moment of these molecules (1.94 and 1.69 D for H_2O and MeOH, respectively). Thus the static properties such as the solvent free energy curve are expected to exhibit similar features. In the same manner, the I.P. in solution for these solvents, which is the net value of the solvation coordinate, have resulted in close values.

D. Dielectric relaxation dynamics

The MD trajectory calculation enables us to investigate the nonequilibrium process of the solvation (dielectric relaxation) as well as the equilibrium properties. First, the configurations ($\mathbf{R}$,$\mathbf{r}$) and velocities ($\dot{\mathbf{R}}$,$\dot{\mathbf{r}}$) of the system, which are to be adopted as the initial condition for the nonequilibrium trajectory calculations, were sampled in the course of the equilibrium run on the neutral potential W_0. We assumed that the emission of an electron from the DMA molecule becomes possible when the potential energies of two states the cation potential $W_1(\mathbf{R},\mathbf{r})$ and the photon dressed neutral potential $W_0(\mathbf{R},\mathbf{r}) + V_{\text{photon}}$ coincide with each other. Thus the configurations and velocities were sampled when the solvation coordinate s satisfied the condition

$$s = W_1(\mathbf{R},\mathbf{r}) - [W_0(\mathbf{R},\mathbf{r}) + V_{\text{photon}}] = 0. \qquad (3.21)$$

The photon energy V_{photon} was taken so that the crossing point locates at the thermal threshold (Fig. 6). The values are 6.0 and 6.6 eV for water and methanol solvent, respectively. In many of the previous calculations on the dynamics of solvent relaxation induced by the ionization or excitation of solute species, the initial conditions had been sampled randomly from the equilibrium trajectories on the ground state surface. The procedure presented here would be more realistic in describing the ionization process in solution than those employed before. Furthermore, it is appropriate for our aim to study the dielectric relaxation process in connection with the electron transfer reaction. About 30 configurations were sampled with at least a 1 ps interval in order to obtain mutually independent ones. In the course of these nonequilibrium simulation calculations, the temperature in the simulation box has increased by 9–10 K for both systems.

Figures 7–9 show the nonequilibrium simulation results. In addition to the solvation coordinate $s(t)$, we have examined the radial component of the polarization $P_r(t)$:

$$P_r(t) = \sum_i \boldsymbol{\mu}_i \cdot \mathbf{u}_i(t), \qquad (3.22)$$

where $\boldsymbol{\mu}_i$ denotes the dipole unit vector of the ith solvent molecule and $\mathbf{u}_i$ is the unit vector directed from the center of mass of DMA to that of the ith solvent molecule. The polarization $P_r(t)$ thus defined extracts the orientational relaxation of the solvent dipole under the electrostatic field from DMA$^+$ separating out the translational component of relaxation. This is also related to the traditional dielectric continuum approximation.

In examining these variables, we have divided the contributions from solvent molecules into first and second shell conponents. Shell boundaries were defined using the minima (r_{shell}) in the radial distribution function between the centers of mass of neutral DMA and solvent molecules (Sec. III B). The first shell is defined by $0 < r < r_{\text{shell}}$ and the second shell by $r_{\text{shell}} < r < L/2$, where L is the simulation box length. Dividing the shell contributions, the polarization $P_r(t)$ was normalized by the shell width Δr. Assuming the homogeneous dipolar solvent, the number of solvent dipoles in the shell region between r and $r + \Delta r$ increase proportionally to $r^2[n(r)\Delta r = \rho 4\pi r^2 \Delta r]$ and the ion–dipole pair interaction energy is proportional to $1/r^2$ ($V_{\text{ion-dipole}} = q\mu \cos\theta / r^2$), where r is the distance between an ion and a point dipole. Therefore, it would be proper to normalize the contributions from the solvent shell by Δr

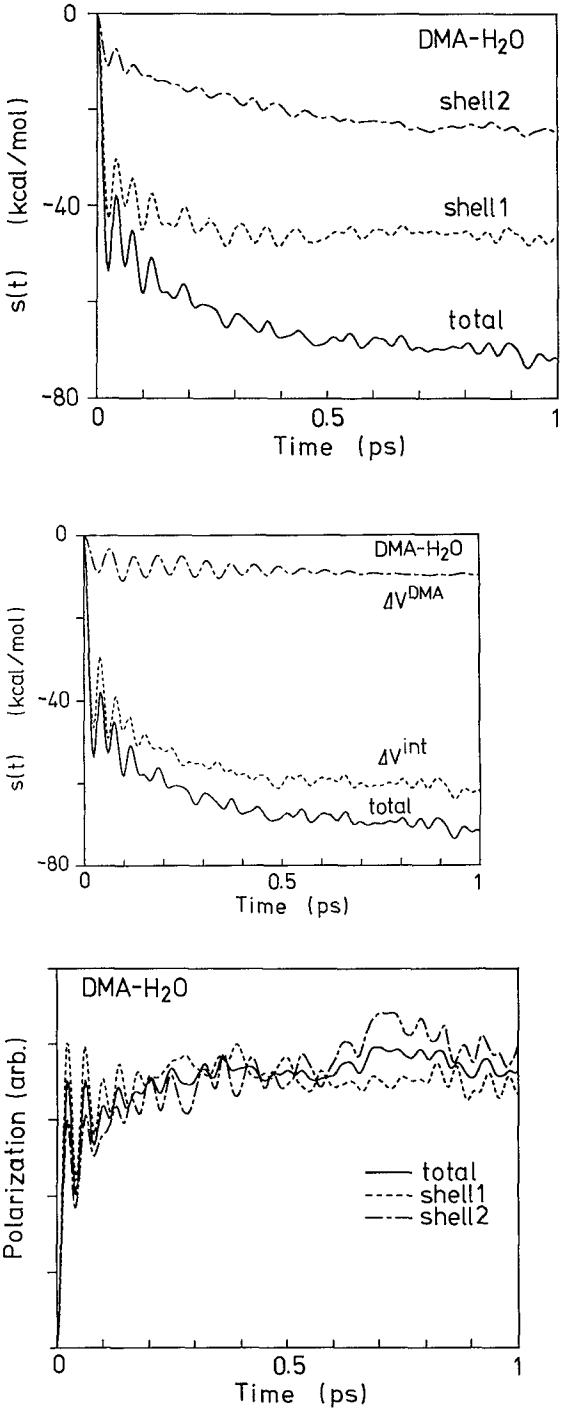

FIG. 7. Nonequilibrium simulation results for the DMA–H_2O solution. (a) Solvent shell components of the solvation coordinate $s(t)$. (b) $s(t)$ divided into the inter- and intramolecular terms. (c) Solvent shell components of the polarization $P_r(t)$. In (a), (b), and (c), solid lines are total $s(t)$ or $P_r(t)$. Dashed and dashed–dotted lines correspond to first and second shell components in (a) and (c), and to $V_1^{\text{int}} - V_0^{\text{int}}$ and $V_1^{\text{DMA}} - V_0^{\text{DMA}}$ in (b).

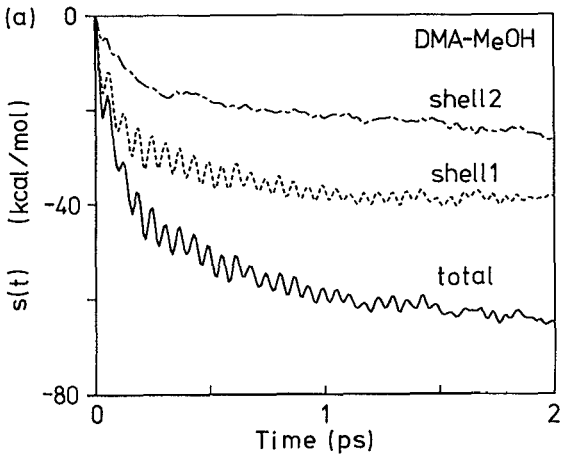

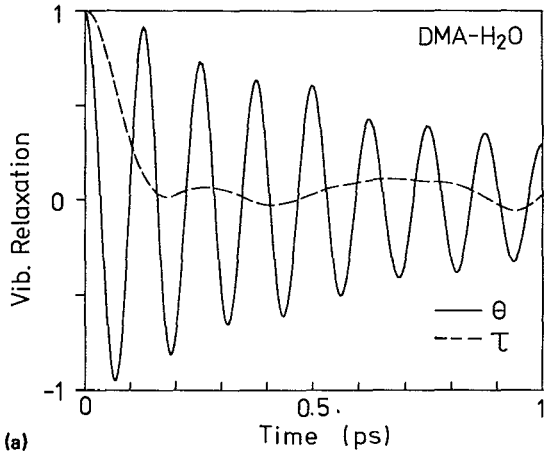

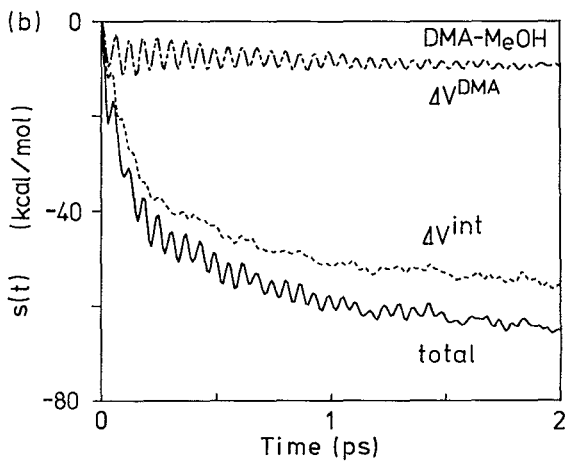

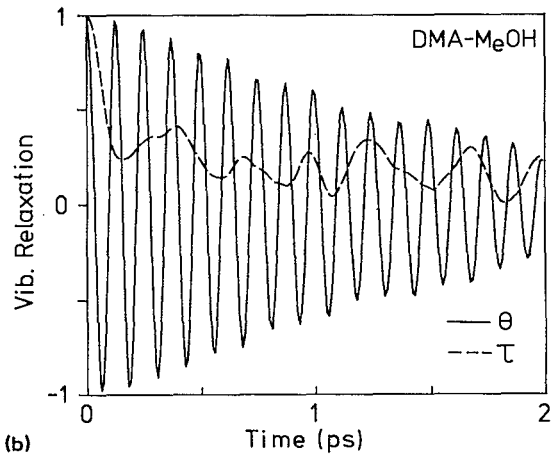

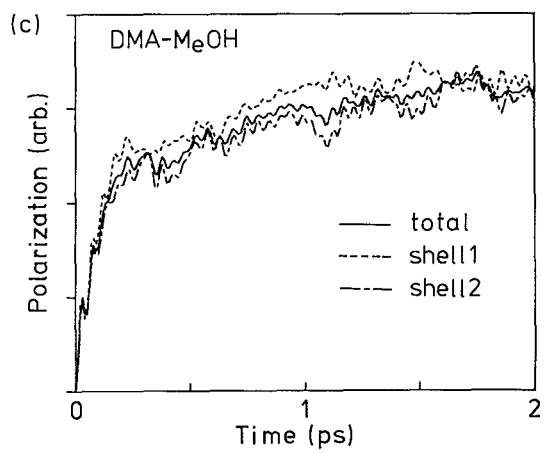

FIG. 8. Nonequilibrium simulation results for the DMA–MeOH solution. (a), (b), and (c) are similar to Fig. 7.

FIG. 9. Vibrational relaxation of θ and τ in (a) water and (b) methanol solutions. Solid and dashed lines correspond to θ and τ, respectively.

when examining $P_r(t)$ in relation to the continuum approximation. The shell widths of the first and second shells were $\Delta r_1 = r_{\text{shell}} - r_{\text{DMA}}$ and $\Delta r_2 = L/2 - r_{\text{shell}}$, respectively. The value for r_{DMA} was taken as 4.0 Å (Sec. II C). In Figs. 7(b) and 8(b), the solvation coordinate $s(t)$ was also divided into two components $V_1^{\text{int}} - V_0^{\text{int}} = \Delta V^{\text{int}}$ and $V_1^{\text{DMA}} - V_0^{\text{DMA}} = \Delta V^{\text{DMA}}$. The nonequilibrium simulation results shown in Figs. 7–9 are the averaged ones over 30 trajectories.

Figures 7(a) and 7(b) monitor the nonequilibrium relaxation of $s(t)$ in the DMA–H_2O system. As seen in the figure, it exhibits a fast relaxation on a time scale of 0.1–0.2 ps and attendant remarkable oscillations with characteristic frequency of about 830 cm^{-1}. This oscillatory behavior comes mainly from the solute–solvent interaction term (ΔV^{int}). Figure 7(c), which shows the response of the polarization $P_r(t)$, suggests that this oscillation in $s(t)$ can be attributed to the librational mode of the solvent water molecules. The first shell solvent molecules dominate the fast and oscillatory relaxation of $s(t)$. However, the second shell component is not negligible. The librational oscillation in the second shell occurs coherently to that in the first shell [Fig. 7(c)] and the slowly relaxing tail ($t > 0.3$ ps) in the total relaxation of $s(t)$ seems to be dominated by the second shell component. The coherent excitation of the libration is due to the long-ranged nature of the solvent–solvent interaction. Such behavior is commonly observed in the studies of the liquid water.[20–23]

Figure 8 displays the response of the DMA–MeOH system. Compared to the case of the water solvent, the DMA–MeOH system shows slower decay on a time scale of 0.5–0.7 ps with less oscillatory behavior. The small oscillation accompanying to the relaxation of the total $s(t)$ comes from the component ΔV^{DMA}, the contribution from the intramolecular vibration of the solute DMA. It should be noted that we have treated only two internal degrees of freedom θ and τ explicitly. Thus the intra- and intermolecular vibration–vibration (V–V) energy transfer, which may occur in a picosecond, was not incorporated (see Sec. III A). It can therefore be presumed that the relaxation of the real DMA–MeOH system exhibits more overdamped behavior. The response of the polarization $P_r(t)$ in the DMA–MeOH system is presented in Fig. 8(c). As seen in the figure, a small librational oscillation occurs in the very initial stage of the relaxation in this system too. However, the excitation of libration is weak and the reorientation of the methanol solvent shows a much overdamped relaxation compared with the case of the water solvent. We can see in Fig. 8(a) that the second shell component of the relaxation of $s(t)$ in the DMA–MeOH system is comparable to that of the first shell, in contrast to the DMA–H_2O system in which the fast initial relaxation is dominated largely by the first solvent shell [Fig. 7(a)].

Some molecular theories of solvation predict the multiexponential decay for the dielectric relaxation.[14–16] These time constants have been attributed to the shell contributions from the nearest-neighbor solvent molecules to the distant bulk solvent. The collective relaxation of the bulk solvent was expected to be fast with the time constant of the longitudinal dielectric relaxation time τ_L and the slower component of relaxation was assumed to come from the reorientation of solvent molecules in the vicinity of the solute (Onsager's snowball picture).[14–16,45] The simulation results shown in Figs. 7–8 indicate that these models or pictures do not adequately describe the relaxation dynamics of the present system. This might be due to the complexities of the present systems especially of the particular forms of the solvent–solvent interaction, which is difficult to be incorporated into those simple models.

It is interesting to compare the shell contributions in $s(t)$ and $P_r(t)$. The distinction between the first and second shells can be seen clearly in the energetic contributions $s(t)$, whereas in the normalized $P_r(t)$, which reflect the reorientation of solvent dipoles, the characteristics of the relaxation dynamics are roughly independent from the solvent shell distance.

E. The vibrational relaxation of the solute DMA

As is expected from the nature of the potential energy surface of DMA and DMA^+ (Fig. 2), the intramolecular vibration of θ and τ will be strongly excited when the ionization of DMA takes place. In order to examine how the vibrational relaxation takes place during the solvation process, we have calculated the autocorrelation functions for the vibrational coordinates θ and τ:

$$\left\langle \frac{x(0)x(t)}{x(0)^2} \right\rangle \quad (x=\theta,\tau), \tag{3.23}$$

where the bracket $\langle\ \rangle$ denotes the average over 30 trajectories. They are shown in Fig. 9.

As seen in the figure, the damping effect is larger in water than in methanol. The relaxation of the vibration of θ exhibits a typical damped oscillation and the time scale of the decay is 0.8–1.0 ps in water and 1.6–1.8 ps in methanol, respectively. However, we found that a sudden stepwise damp is actually induced by the collision of the solvent molecules in each trajectory. The relaxation of the internal rotation τ in water shows a fast (0.1–0.2 ps) and remarkably overdamped decay, whereas in methanol it also exhibits an overdamped behavior, but more irregular motion like a diffusion.

The mechanism of vibrational relaxation in solution has been extensively studied so far.[46–48] The intra- and intermolecular near resonant V–V transfer has been recognized to be important to account for the vibrational relaxation of polyatomic solute molecules in polyatomic solvents as in the present case. It should be kept in mind that we have incorporated only the θ and τ vibrations and ignored the remaining small amplitude vibrations of DMA as well as the vibrational motions of solvent molecules in the present calculations. The relaxation of θ will presumably occur much faster in the real system. However, for the internal rotation τ, the overdamped diffusive nature seen in the present calculations would be appreciably realistic.

IV. DISCUSSION

A. Fluctuation–dissipation relation

It would be important to examine whether the fluctuation–dissipation (FD) relation holds or not even for a realistic system as the present, because many theoretical models[14–19] utilized to analyze the experimental results are based on the LR assumption. With the definition (3.8), we can see the following relation:

$$H_0 = T + W_0 = H_1 - s \ \text{ or } \ H_1 = H_0 + s, \tag{4.1}$$

where H_0 and H_1 denote the Hamiltonian of the system containing DMA and DMA^+, respectively. The solvation coordinate s can be considered formally as a perturbation.

Figure 10 shows the comparison between the nonequilibrium response function and the equilibrium time correlation function of s. The response functions are similar to those presented in Figs. 7–8, but normalized as

$$S(t) = \frac{\langle s(t)\rangle - \langle s(\infty)\rangle}{\langle s(0)\rangle - \langle s(\infty)\rangle}, \tag{4.2}$$

where the braket $\langle\ \rangle$ denotes the average over nonequilibrium trajectories, but $\langle s(\infty)\rangle$ was computed from the equilibrium simulation on W_1. The normalized time correlation functions are given by

$$C_I(t) = \frac{\langle s(0)s(t)\rangle_I - \langle s(0)\rangle_I^2}{\langle s(0)^2\rangle_I - \langle s(0)\rangle_I^2} = \frac{\langle \delta s(0)\delta s(t)\rangle_I}{\langle \delta s(0)^2\rangle_I} \quad (I=0,1), \tag{4.3}$$

where $I=0$ and 1 correspond to the equilibrium simulations on the neutral and cation potential surfaces, respectively.

As seen in the figure, the relaxation of the DMA–H_2O system follows the FD relation to a good approximation. A

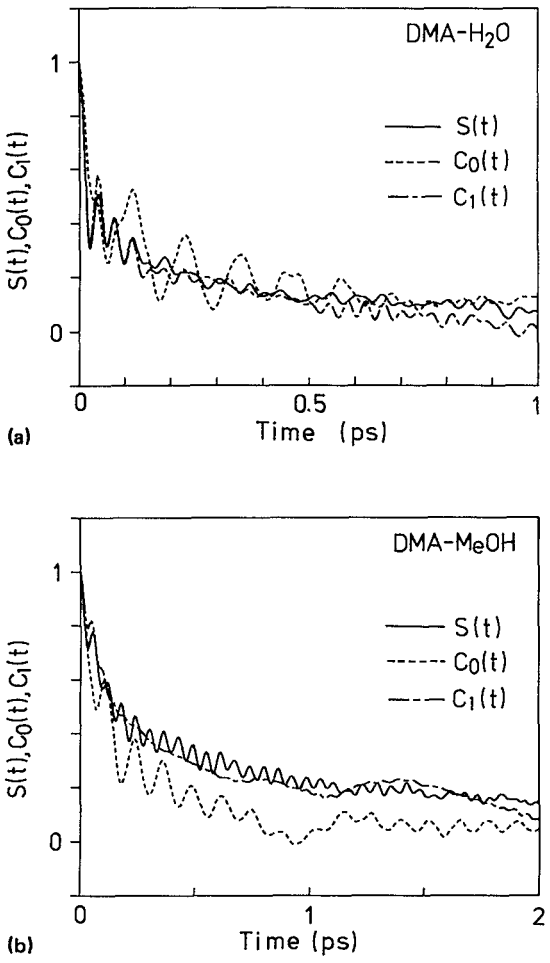

FIG. 10. A comparison between the nonequilibrium response function $S(t)$ and the equilibrium time correlation functions $C_0(t)$ and $C_1(t)$ for (a) DMA–H_2O and (b) DMA–MeOH solutions. Solid, dashed, and dashed–dotted lines correspond to $S(t)$, $C_0(t)$ and $C_1(t)$, respectively.

large amplitude oscillation with a frequency of about 250 cm^{-1} observed in $C_0(t)$ comes from the component of the intramolecular potential V^{DMA}. Taking this into account and focusing on the solvent contribution, the agreement among $S(t)$, $C_0(t)$, and $C_1(t)$ in aqueous solutions can be considered reasonablly well. In particular, the coincidence between $S(t)$ and $C_1(t)$ is remarkable, both of which exhibit the fast initial relaxation accompanying a characteristic oscillation [libration of water (see Sec. III D)].

The acceptability of LR theory in aqueous solution observed here is consistent with the previous works. Maroncelli and Fleming[21] examined the FD relation for the system containing a simple spherical ion in the solvent water cluster. They also studied the solute size dependence of the dynamics and found that the larger solute satisfies LR to better approximation, naturally because the electrostatic perturbation becomes smaller. The relaxation dynamics just after a ferric–ferrous electron transfer in an aqueous solution was *calculated* by Bader and Chandler.[23] They observed that the LR is also well satisfied despite that the solute species are highly charged small ion (Fe^{2+} and Fe^{3+}). The present results indicate that the aqueous solution follows the LR relation even when the solutes are polyatomic molecules having the multipole moments and the large amplitude vibrational modes. It is particularly interesting that $S(t)$ and $C_1(t)$ in the DMA–H_2O system coincide well with each other including the remarkable oscillation due to the libration of water. This characteristic of the librational oscillation was not averaged out by the complexities of the polyatomic organic solute.

It seems rather difficult to judge the validity of LR for the case of the DMA–MeOH system. As seen in Fig. 10(b), the time correlation function for the cation state $C_1(t)$ agrees well with the response function $S(t)$ except for the small oscillation of $S(t)$ coming from the wagging vibration of solute DMA^+. However, a deviation between $C_0(t)$ and $S(t)$ is observed to some extent. We may say that the LR relation obtained for the cation state is because the response function $S(t)$ was calculated from the nonequilibrium trajectories on the same potential surface W_1 as $C_1(t)$ and the perturbation $-s$ in Eq. (4.1) can be regarded to be small. It should be noted that Fonseca and Ladanyi[25] have shown that the LR breaks down clearly for a model diatomic molecule in methanol. Considering this, further studies will be apparently required for methanol.

B. Generalized Langevin analyses

We examined the dynamics of dielectric relaxation processes by representing it as the propagation of systems along the solvation coordinate s which was defined by the difference of the potential energies of two states. Such motion can be described by the stochastic equation of motion because it is regarded as the projection of complicated interactions in solutions onto one-dimensional motion. It would be meaningful to derive the stochastic equations of s for the processes including the surface hopping as in the present case.

For the surface hopping, the crossing of potential surfaces plays a critical role. It is natural to choose the transition state point to be the minimum energy point on the crossing surface

$$f(\mathbf{x}) = W_1(\mathbf{x}) - W_0(\mathbf{x}) = 0, \tag{4.4}$$

where $\mathbf{x}$ is the coordinate and the reaction coordinate to be the steepest descent path passing through this point in the mass-weighted Cartesian coordinate space. With this definition, we obtain two branches of reaction coordinates, one on the surface $W_0(\mathbf{x})$ and the other on $W_1(\mathbf{x})$. It is proved easily that the directions of these two branches coincide with each other and are normal to the crossing surface at the minimum energy point.[31(a)] We can therefore use the reaction coordinate and the normal coordinates perpendicular to it to describe the dynamics near the transition state.

As seen above, the free energy curves are almost parabolic along the solvation coordinate and the LR relation seems to be satisfied at least qualitatively. It would therefore be worth examining the harmonic model in describing the dynamics of the present systems. The potential energies are then expressed as

$$W_I(\mathbf{x}) = \sum_i \frac{1}{2}\omega_i^2 x_i^2 + \sum_i g_i^I x_i + W_I(\mathbf{0}) \quad (I=0,1), \tag{4.5}$$

where the photon energy V_{photon} is included in $W_0(\mathbf{0})$. For these potential functions, the minimum energy crossing point $\mathbf{x}^\ddagger$ is given by

$$x_i^\ddagger = \omega_i^{-2}\left\{\sum_j \omega_j^{-2}(g_i^0 g_j^1 - g_i^1 g_j^0)(g_j^0 - g_j^1) + (g_i^0 - g_i^1) \times [W_1(\mathbf{0}) - W_0(\mathbf{0})]\right\} \Big/ \left[\sum_j \omega_j^{-2}(g_j^0 - g_j^1)^2\right] \tag{4.6}$$

and the direction vector of reaction coordinate $^t\tilde{\mathbf{s}} = (\tilde{s}_1, \tilde{s}_2, \ldots)$ by

$$\tilde{s}_i = \frac{dx_i}{d\tilde{s}} = \frac{\Delta g_i}{(\Sigma_j \Delta g_j^2)^{1/2}}, \tag{4.7}$$

with

$$\Delta g_i = g_i^1 - g_i^0.$$

If we take the coordinate $\tilde{s}$ as a linear line with the direction of $\tilde{\mathbf{s}}$,

$$\tilde{s} = {}^t\tilde{\mathbf{s}}\cdot\tilde{\mathbf{x}}, \tag{4.8}$$

where $\tilde{\mathbf{x}}$ is the displacement measured from the minimum energy crossing point

$$\tilde{\mathbf{x}} = \mathbf{x} - \mathbf{x}^\ddagger. \tag{4.9}$$

As is easily seen, the potential energy difference of two states is proportional to the coordinate $\tilde{s}$ defined here

$$s = W_1(\mathbf{x}) - W_0(\mathbf{x}) = (\sum_j \Delta g_j^2)^{1/2}\tilde{s}. \tag{4.10}$$

It is straightforward to derive the GLE for the motion along the energy difference coordinate s. Using the projection operator $\hat{\mathbf{P}}$ with the element

$$\hat{P}_{ij} = \Delta g_i \Delta g_j / \sum_k \Delta g_k^2, \tag{4.11}$$

and the usual matrix partitioning technique with $\hat{\mathbf{Q}} = \mathbf{I} - \hat{\mathbf{P}}$, the resultant GLE is derived as

$$\ddot{s} + [\bar{\omega}^2 - \zeta(0)]s + \mu^{-1/2}\bar{g} + \int_0^t \zeta(\tau)\dot{s}(t-\tau)d\tau + \zeta(t)s(0) = \mu^{-1/2}R(t), \tag{4.12}$$

where μ is the factor connecting the coordinate $\tilde{s}$ and the solvation coordinate s, $\mu^{-1/2} = (\Sigma_k \Delta g_k^2)^{1/2}$ and may be regarded as the effective mass [see Eq. (4.18) below]. The friction kernel $\zeta(t)$ is given formally as

$$\zeta(t) = \tilde{\omega}_{PQ}^2 \tilde{\omega}_{QQ}^{-2}\cos(\tilde{\omega}_{QQ}t)\tilde{\omega}_{QP}^2 \tag{4.13}$$

and is related to the random force $R(t)$ by the second FD theorem

$$\langle R(0)R(t)\rangle = \zeta(t)k_B T. \tag{4.14}$$

In Eq. (4.12), the average quantities $\bar{\omega}^2$ and $\bar{g}$ are

$$\bar{\omega}^2 = \sum_k \omega_k^2 \tilde{s}_k^2, \tag{4.15}$$

and

$$\bar{g} = \sum_k (g_k^I + \omega_k^2 x_k^\ddagger)\tilde{s}_k, \tag{4.16}$$

respectively. The elements of column vector $\tilde{\omega}_{QP}^2$ and matrix $\tilde{\omega}_{QQ}^2$ are given by

$$\tilde{\omega}_{QP,i}^2 = (\omega_i^2 - \bar{\omega}^2)\tilde{s}_i, \tag{4.17a}$$

$$\tilde{\omega}_{QQ,ij}^2 = \omega_i^2\delta_{ij} + (\bar{\omega}^2 - \omega_i^2 - \omega_j^2)\tilde{s}_i\tilde{s}_j. \tag{4.17b}$$

The raw vector $\tilde{\omega}_{PQ}^2$ is the transpose of $\tilde{\omega}_{QP}^2$. It is noted that the projected frequency matrix $\tilde{\omega}_{QQ}^2$ has only one zero eigenvalue corresponding to the motion along $\tilde{s}$.

The present MD calculations provide several quantities in the GLE (4.12). The components of direction vector $\tilde{\mathbf{s}}$ are related to the velocity autocorrelation function

$$\langle \dot{s}(0)\dot{s}(t)\rangle = \frac{k_B T}{\mu}\sum_i \tilde{s}_i^2 \cos\omega_i t. \tag{4.18}$$

Figure 11 shows the components of $\tilde{\mathbf{s}}$, $\tilde{s}_i$, computed from the Fourier transform of the correlation functions for the cation state. The components $\tilde{s}_i$ of the DMA–H_2O system exhibits a band at about the 750–900 cm^{-1} region and a small hump at about 600 cm^{-1}. The former consists of the librational mode of water. A flat tail at the low frequency region can also be seen, which would be the contribution from the translational mode. The component $\tilde{s}_i$ of the DMA–MeOH system has a main band centered at about 650 cm^{-1}, the librational mode of the methanol O–H part. There also exist certain components at the small frequency region with a hump at about 100–150 cm^{-1}. As seen in Fig. 11, the main band for the water solution is composed of several separated narrow peaks while that for the methanol solution does not have distinguished structures. This result comes from the oscillatory nature of H_2O relaxation dynamics observed in Fig. 7. Although we can make some physical speculation on the origin of each mode, detailed information will be obtained by the analyses of the potential surfaces around the crossing seam.

Once we have obtained the components $\tilde{s}_i$, the frequency components of the friction kernel $\zeta(t)$ can be computed straightforwardly. The matrix $\tilde{\omega}_{QQ}^2$ [Eq. (4.17)] was first diagonalized and the vectors $\tilde{\omega}_{QP}^2$ and $\tilde{\omega}_{PQ}^2$ were then unitary transformed using the eigenvectors corresponding to the

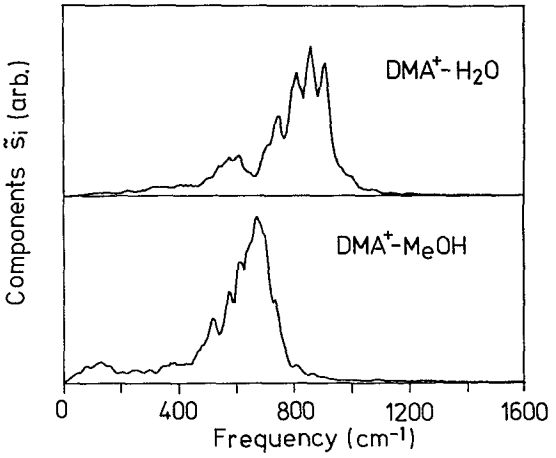

FIG. 11. Components of the reaction coordinate vector $\tilde{s}_i^2$ and frequencies ω_i of DMA^+–H_2O (upper) and DMA^+–MeOH (lower).

nonzero eigenvalues. By this procedure, the friction kernel $\zeta(t)$ was expressed as

$$\zeta(t) = \sum_i \frac{(\omega^2_{PQ,i})^2}{\omega^2_{QQ,i}} \cos(\omega_{QQ,i}t) = \sum_i \hat{\zeta}(\omega_{QQ,i}) \times \cos(\omega_{QQ,i}t), \tag{4.19}$$

where $\omega^2_{QQ,i}$ is the eigenvalue and $\omega^2_{PQ,i}$ is the component of the transformed vector. The resultant friction kernels both for H_2O and MeOH solutions are displayed in Fig. 12.

We obtain the effective frequency Ω for the harmonic free energy curve by

$$\Omega^2 \equiv \overline{\omega}^2 - \zeta(0) = \overline{\omega}^2 - \sum_i \frac{(\omega^2_{PQ,i})^2}{\omega^2_{QQ,i}} \tag{4.20}$$

and they are calculated to be 417 and 196 cm^{-1} for H_2O and MeOH solutions, respectively. It is pointed out that the effective frequency Ω can also be calculated directly from the equilibrium MD simulations with the Gaussian approximation

$$\Omega = [\langle \delta\dot{s}(0)^2 \rangle / \langle \delta s(0)^2 \rangle]^{1/2} \tag{4.21}$$

and the resultant frequencies Ω are 440 and 190 cm^{-1} for H_2O and MeOH, respectively, which are in good agreement with the values from Eq. (4.20). The effective mass μ was calculated to be 0.42×10^{-4} and 1.99×10^{-4} $ps^2\,eV^{-1}$ for H_2O and MeOH solutions, respectively. In Sec. III C, the force constants of the free energy curves were found to have close values in these two solvents reflecting the static interaction energies. The difference of the relaxation times between them can be ascribed to the values of the effective mass. As can be seen easily, the obtained values of μ, Ω, and the force constants presented in Sec. III C are consistent with each other.

The present GLE analyses provide important insight into the mechanism of dielectric relaxation of the present systems. As seen in Fig. 12, the time-dependent friction $\zeta(t)$ for the MeOH solution falls off very rapidly and is followed by an oscillation with a very low frequency ~ 167 cm^{-1} and the time scale of the initial decay of $\zeta(t)$ is much shorter than that of the dielectric relaxation shown in Fig. 8. In such a case, the relaxation dynamics can be described by the Langevin equation (LE) at least qualitatively in which the friction kernel is approximated by

$$\zeta(t) = \bar{\zeta}\delta(t) \tag{4.22a}$$

and

$$\bar{\zeta} = \int_0^\infty \zeta(t)dt. \tag{4.22b}$$

The overdamped behavior observed in Fig. 8 may be interpreted from this result because an overdamped relaxation dynamics is characterized by the LE description. In contrast to the methanol solution, the time-dependent friction of aqueous solution decays with the time scale comparable to that of the relaxation dynamics (Fig. 7) and shows a very long tail as seen in Fig. 12. In such a situation, the dynamics may be well understood by the converted form of GLE

$$\ddot{s} + \overline{\omega}^2 s - \int_0^t \dot{\zeta}(\tau)s(t-\tau)d\tau + \mu^{-1/2}\bar{g} = \mu^{-1/2}R(t), \tag{4.23a}$$

where

$$\dot{\zeta}(t) = \tilde{\omega}^2_{PQ}\tilde{\omega}^{-1}_{QQ}\sin(\tilde{\omega}_{QQ}t)\tilde{\omega}^2_{QP} \tag{4.23b}$$

and the short time dynamics will be dominated by the potential with the frequency $\sqrt{\overline{\omega}^2}$. Using Eq. (4.15), the frequency was calculated to be 794 cm^{-1}, which is close to the characteristic frequency for the oscillatory behavior observed in the DMA^+–H_2O solution.

Apparently, more careful analysis will be needed in order to elucidate the detailed mechanism of solvation dynamics. In principle, specific characteristics should be solely contained in the GLE form (provided that the harmonic assumption is valid). Above all, the nature of the friction kernel $\zeta(t)$ will play a critical role. Although we have performed at present a simple analysis using the time progression of the solvation coordinate $s(t)$ computed from the equilibrium MD simulation, more direct information will be achievable by the analyses of the potential energy surfaces on the basis of the GLE formalism presented here.

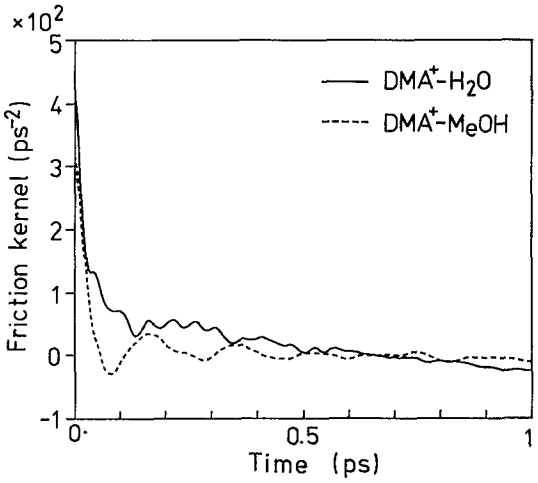

FIG. 12. Time-dependent friction kernel $\zeta(t)$ in units of ps^{-2}. Solid and dashed lines correspond to DMA^+–H_2O and DMA^+–MeOH solutions, respectively.

V. SUMMARY AND CONCLUSION

In the present work, we have carried out the MD trajectory calculations on DMA in water and methanol solutions to explore the mechanism of dielectric relaxation dynamics induced by the ionization of DMA. The potential energy surface of DMA and the interaction potentials with the solvent molecules were derived from the *ab initio* MO calculations on DMA and DMA–H_2O systems. Although we focused on the ionization of DMA, the results obtained here would provide important information on the photoinduced electron transfer reactions because DMA is a prototype of donor molecules in those reactions. For intermolecular electron transfer with a large donor–acceptor distance, the solvation dynamics associated with electron transfer can be described as a convolution of dynamics of donor and acceptor systems. We are now working on the dynamics of photoin-

duced electron transfer reactions as an extension of the present work.

The dielectric relaxation dynamics has been analyzed in terms of the free energy curves of solvations; the potentials of mean force for the solvation coordinate defined by the difference of potential energies. It was found that the free energy curves are almost parabolic both for the aqueous and methanol solutions and nonlinear effects such as the dielectric saturation were not observed in the present case. The static energy relations were also found to be very similar in both solutions as expected from the dielectric constants of H_2O and MeOH.

The dynamical behaviors of these two solvents were much different from each other. For the aqueous solution, the dielectric relaxation was very fast on the time scale of 0.1–0.2 ps and a remarkable oscillation with the frequency of about 830 cm^{-1}, ~0.04 ps, was observed. A large part of energy relaxation is achieved in the period of the initial oscillation. On the other hand, any notable oscillation originated from the solvent motion was not seen in the relaxation dynamics of methanol solution. The time scale of solvation 0.7–0.8 ps was slower than that of the H_2O case. It should be noted, however, that the dielectric relaxation of methanol is generally slow considering the longitudinal dielectric relaxation time τ_L of ~8 ps. The present calculations revealed that there is a very fast time scale even for MeOH and the relaxation with this time scale accounts for the major part of the potential energy lowering in the relaxation process.

In order to obtain a deeper insight into the dielectric relaxation dynamics treated by the present MD calculations, we have derived the GLE for the case of surface hopping. The harmonic potentials were assumed because the free energy curves are almost parabolic and the LR relation seems to be a good approximation as discussed in Sec. IV A. In deriving the GLE, we applied the reaction path model for the surface hopping process originally developed in the gas phase photochemical processes. With this model, the components of the solvation coordinate and the friction kernel were deduced from the MD calculations which are important to elucidate the mechanism of dielectric relaxation dynamics. The reaction path model presented here can be constructed from the potential energy surface of solute–solvent systems and will provide useful information on the nature of the coupling between the solvation coordinate and the bath modes. We are now planning to proceed with the work along this line.

ACKNOWLEDGMENTS

The authors are grateful to Professor I. Ohmine for stimulating discussions. Numerical calculations were carried out at the Computer Center of the University of Tokyo, IMS Computer Center, and Data Processing Center of Kyoto University. This work was supported by the Grants in Aid for Scientific Research from the Ministry of Education.

[1] P. G. Wolynes, Annu. Rev. Phys. Chem. **31**, 345 (1984).
[2] P. Madden and D. Kivelson, Adv. Chem. Phys. **66**, 467 (1986).
[3] E. M. Kosower and D. Huppert, Annu. Rev. Phys. Chem. **37**, 127 (1986).
[4] P. F. Barbara and W. Jarzeba, Acc. Chem. Res. **21**, 195 (1988); Adv. Photochem. **15**, 1 (1990).
[5] G. E. McManis and M. J. Weaver, Acc. Chem. Res. **23**, 294 (1990).
[6] R. A. Marcus, J. Chem. Phys. **24**, 966 (1956); **24**, 979 (1956); Annu. Rev. Phys. Chem. **15**, 155 (1964).
[7] M. D. Newton and M. Sutin, Annu. Rev. Phys. Chem. **35**, 437 (1984).
[8] J. T. Hynes, in *The Theory of Chemical Reaction Dynamics*, edited by M. Baer (CRC, Boca Raton, Florida, 1985), Vol. 4, p. 171.
[9] (a) J. K. Hwang and A. Warshel, J. Am. Chem. Soc. **109**, 715 (1987); (b) A. Warshel and J. K. Hwang, J. Chem. Phys. **84**, 4938 (1986); (c) G. King and A. Warshel, *ibid.* **93**, 8682 (1990).
[10] R. B. Barnett, U. Landman, and A. Nitzan, J. Chem. Phys. **90**, 4413 (1989).
[11] A. Yoshimori, T. Kakitani, Y. Enomoto, and N. Mataga, J. Phys. Chem. **93**, 8316 (1989).
[12] S. Kato and Y. Amatatu, J. Chem. Phys. **92**, 7241 (1990).
[13] E. A. Carter and J. T. Hynes, J. Chem. Phys. **94**, 5961 (1991).
[14] P. G. Wolynes, J. Chem. Phys. **86**, 5133 (1987).
[15] I. Rips, J. Klafter, and J. Jortner, J. Chem. Phys. **88**, 3246 (1988); **89**, 4288 (1988).
[16] A. L. Nichols III and D. F. Calef, J. Chem. Phys. **89**, 3783 (1988).
[17] D. F. Calef and P. G. Wolynes, J. Chem. Phys. **78**, 4145 (1983).
[18] (a) B. Bagchi and A. Chandra, J. Chem. Phys. **90**, 7338 (1989); (b) A. Chandra and B. Bagchi, J. Phys. Chem. **93**, 6996 (1989).
[19] G. van der Zwan and J. T. Hynes, J. Phys. Chem. **89**, 4181 (1985); J. T. Hynes, *ibid.* **90**, 3701 (1986).
[20] M. Rao and B. J. Berne, J. Phys. Chem. **85**, 1498 (1981).
[21] M. Maroncelli and G. R. Fleming, J. Chem. Phys. **89**, 5044 (1988).
[22] O. A. Karim, A. D. J. Haymet, M. J. Banet, and J. D. Simon, J. Phys. Chem. **92**, 3391 (1988).
[23] (a) J. S. Bader and D. Chandler, Chem. Phys. Lett. **157**, 501 (1989); (b) R. A. Kuharski, J. S. Bader, D. Chandler, M. Spirk, M. L. Klein, and R. W. Impey, J. Chem. Phys. **89**, 3248 (1988); (c) J. S. Bader, R. A. Kuharski, and D. Chandler, *ibid.* **93**, 230 (1990).
[24] M. Maroncelli, J. Chem. Phys. **94**, 2084 (1991).
[25] T. Fonseca and B. M. Ladanyi, J. Phys. Chem. **95**, 2116 (1991).
[26] See, e.g., H. Beens and A. Weller, in *Organic Molecular Photophysics*, edited by J. B. Birks (Wiley-Interscience, London, 1975), Vol. 2, p. 159.
[27] (a) H. Frohlich, *Theory of Dielectrics* (Oxford University, Oxford, 1949); (b) D. Kivelson and H. Friedman, J. Phys. Chem. **93**, 7026 (1989).
[28] G. E. McManis, R. M. Nielson, A. Gochev, and M. J. Weaver, J. Am. Chem. Soc. **111**, 5533 (1989).
[29] (a) M. Maroncelli, J. MacInnis, and G. R. Fleming, Science **243**, 1674 (1989); (b) G. R. Fleming and P. G. Wolynes, Phys. Today **43**, 36 (1990).
[30] M. A. Kahlow, W. T. Jarzeba, T. J. Kang, and P. F. Barbara, J. Chem. Phys. **90**, 151 (1989).
[31] (a) S. Kato, R. L. Jaffe, A. Komornicki, and K. Morokuma, J. Chem. Phys. **78**, 4567 (1983); (b) S. Kato, *ibid.* **88**, 3045 (1988).
[32] We used the program HONDO7 for self-consistent field (SCF) calculations; M. Dupuis, J. D. Watts, H. O. Villar, and G. J. B. Hurst, HONDO version 7.0, QCPE 544, 1987.
[33] (a) W. J. Hehre, R. Ditchfield, and J. A. Pople, J. Chem. Phys. **56**, 2252 (1972); (b) J. S. Binkley, J. A. Pople, and W. J. Hehre, J. Am. Chem. Soc. **102**, 939 (1980).
[34] J. W. Robinson, *Handbook of Spectroscopy* (CRC, Boca Raton, Florida, 1974), Vol. 1.
[35] R. G. Gordon and Y. S. Kim, J. Chem. Phys. **56**, 3122 (1972).
[36] J. W. Smith, J. Chem. Soc. **1961**, 81.
[37] (a) W. L. Jorgensen, J. Phys. Chem. **90**, 1276 (1986); (b) W. L. Jorgensen, J. Chandrasekhar, J. D. Madura, R. W. Impey, and M. L. Klein, J. Chem. Phys. **79**, 926 (1983).
[38] M. Abramowitz and I. A. Stegun, *Handbook of Mathematical Functions* (Dover, New York, 1970).
[39] D. J. Evans and S. Murad, Mol. Phys. **34**, 327 (1977).
[40] See the textbook; M. P. Allen and D. J. Tidesley, *Computer Simulation of Liquids* (Clarendon, Oxford, 1987).
[41] C. W. Gear, *Numerical Initial Value Problems in Ordinary Differential Equations* (Prentice–Hall, Englewood Cliffs, New Jersey, 1971).
[42] D. J. Adams, E. H. Adams, and G. J. Hills, Mol. Phys. **38**, 387 (1979).
[43] E. A. Carter and J. T. Hynes, J. Phys. Chem. **93**, 2184 (1989).
[44] (a) T. Kakitani and N. Mataga, J. Phys. Chem. **89**, 4752 (1985); **90**, 993

(1989); **91**, 6277 (1987); (b) Y. Hatano, M. Saito, T. Kakitani, and N. Mataga, *ibid*. **92**, 1008 (1988).
[45] L. Onsager, J. Am. Chem. Soc. **58**, 1486 (1936).
[46] See, e.g.: (a) D. W. Oxtoby, Adv. Chem. Phys. **47**, 487 (1981); (b) J. Chesnoy and G. M. Gale, *ibid*. **70**, 297 (1988).
[47] I. Ohmine, J. Chem. Phys. **85**, 3342 (1986).
[48] R. M. Whitnell, K. R. Wilson, and J. T. Hynes, J. Phys. Chem. **94**, 8625 (1990), and references therein.